J. Fluid Mech. (2024), *vol*. 984, A44, doi:10.1017/jfm.2024.216

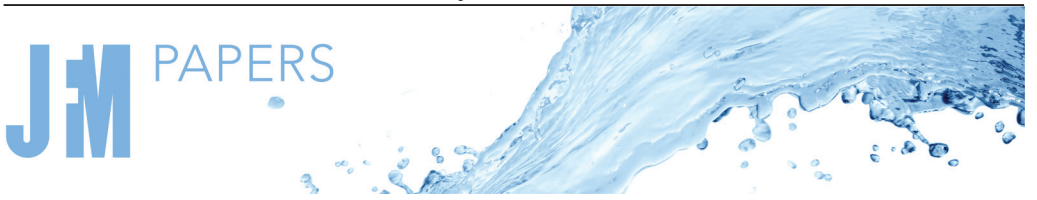

On the generation of near-wall dilatational motions in hypersonic turbulent boundary layers

Ming Yu[1], **ZiSong Zhou**[2], **SiWei Dong**[1], **XianXu Yuan**[1,†] **and ChunXiao Xu**[2,†]

[1]State Key Laboratory of Aerodynamics, Mianyang 621000, PR China

[2]Key Laboratory of Applied Mechanics, Ministry of Education, Institute of Fluid Mechanics, Department of Engineering Mechanics, Tsinghua University, Beijing 100084, PR China

(Received 22 August 2023; revised 26 February 2024; accepted 27 February 2024)

Dilatational motions in the shape of travelling wave packets have been identified recently to be dynamically significant in hypersonic turbulent boundary layers. The present study investigates the mechanisms of their generation and their association with the solenoidal motions, especially the well-recognized near-wall self-sustaining process of the regeneration cycle between the velocity streaks and quasi-streamwise vortices. By exploiting the direct numerical simulation databases and orchestrating numerical experiments, we explore systematically the near-wall flow dynamics in the processes of the formation and transient growth of low-speed streaks. We conclude via theoretical ansatz that the nonlinearity related to the parallel density and pressure gradients close to the wall due to the restriction of the isothermal boundary condition is the primary cause of the generation of the dilatational structures at small scales. In fully developed turbulence, the formation and the existence of healthy dilatational travelling wave packets require the participation of the turbulence at scales larger than those of the near-wall regeneration cycles, especially the occurrence of the bursting events that generate vortex clusters. This is proven by the less intensified dilatational motions in the numerical experiments in which the Orr mechanism is alleviated and the vortical structures and turbulent bursts are weakened.

Key words: compressible boundary layers, turbulent boundary layers

1. Introduction

Hypersonic turbulent boundary layers have become a topic of great interest amongst researchers in the fluid dynamics community due to their significant engineering applications (Gatski & Bonnet 2013; Theofilis, Pirozzoli & Martin 2022). With the aid of advanced experimental equipment and apparatus, and powerful computational resources,

† Email addresses for correspondence: yuanxianxu@cardc.cn, xucx@tsinghua.edu.cn

abundant databases have been established for the purpose of accurate predictions of the aerodynamic performance of high-speed vehicles (Roy & Blottner 2006; Tichenor, Humble & Bowersox 2013; Williams *et al.* 2018; Ceci *et al.* 2022; Huang, Duan & Choudhari 2022). Compared with incompressible flows, a crucial aspect that complicates the modelling and prediction of hypersonic turbulence is the compressibility effects (Smits & Dussauge 2006; Duan, Beekman & Martin 2010, 2011), encompassing the influences caused by the variation of mean fluid properties (density and viscosity, for instance) due to aerodynamic heating, and the fluctuations of density and velocity divergence related to compression and expansion of the fluid elements (Gatski & Bonnet 2013). It has been pointed out by the well-known Morkorvin hypothesis (Morkovin 1962) that the statistics in turbulent boundary layers without strong pressure gradients at free-stream Mach number lower than 5 manifest no evident deviation from those of the incompressible flows to the extent that the effects of mean density and viscosity variations are incorporated appropriately (Griffin, Fu & Moin 2021). This has been validated by previous studies (Duan *et al.* 2011; Cogo *et al.* 2022), in that the van Driest transformed mean velocity (Bernardini & Pirozzoli 2011; Pirozzoli & Bernardini 2011) and the density-weighted Reynolds stress are consistent with those of incompressible flows, even when the free-stream Mach numbers are as high as 12 (Duan *et al.* 2011) and 20 (Lagha *et al.* 2011).

The genuine compressibility effects associated with the dilatational motions, on the other hand, were not commonly regarded as a subject of any great importance. It was not until the utilization of the Helmholtz decomposition in hypersonic turbulent boundary layers at Mach numbers higher than 6 that the contributions of the dilatational motions to the mean skin friction and the Reynolds shear stress were evaluated quantitatively to be finite levels of approximately 5 % and 10 %, respectively (Yu, Xu & Pirozzoli 2019; Yu & Xu 2021). The pressure fluctuations, in comparison, are significantly enhanced and proportional to the square of the Mach number (Yu, Xu & Pirozzoli 2020) in turbulence over adiabatic walls, with further increases in the presence of cooling walls (Zhang *et al.* 2022). Xu *et al.* (2021*b*) found that the dilatational motions are responsible for the inter-scale energy transfer in the near-wall region, with the compressive and expansive motions contributing markedly to the direct and reverse energy transfer, respectively. Recent studies by Yu *et al.* (2022*a*,*b*) have systematically investigated the statistics and flow structures of the wall shear stress and heat flux fluctuations at different Mach numbers and wall temperatures, revealing that the root-mean-square of these two flow quantities increases monotonically with increasing friction Mach numbers, and that the spectra intensities at the mid-frequency range are gradually increasing and manifesting as secondary peaks. These findings highlight the importance of incorporating compressibility effects in the modelling and prediction of hypersonic turbulence.

The above-mentioned phenomena pertain to the emergence and predominance of dilatational structures, which are organized in the form of streamwise alternating positive and negative patterns within the viscous sublayer (Zhang *et al.* 2022), known as the 'travelling wave packets' (TWPs) (Yu *et al.* 2019). These structures are spatially associated with low-speed streaks and strong vortical clusters (Yu & Xu 2021; Yu *et al.* 2022*b*). Despite their crucial role, the origin of the dilatational motions in the form of TWPs remains unclear, as do their dynamical correlations with the vortical motions that populate the near-wall turbulence. This serves as the motivation for the present study. In this paper, we investigate the generation mechanisms of the dilatational TWP structures by exploiting direct numerical simulations (DNS) databases, conducting numerical experiments in minimal flow units (Schoppa & Hussain 2002; Deng & Xu 2012), and analysing theoretically the governing equation of the velocity divergence. Considering that the

dilatational TWP structures lie primarily close to the wall, we scrutinize each stage of the most crucial dynamic processes in the near-wall region, namely the regeneration cycle between the velocity streaks and streamwise vortices, to trace the generation of the dilatational motions and their interaction with the solenoidal vortical ones.

The rest of the paper is organized as follows. Section 2 presents the morphology and kinetic depictions of the dilatational motions via the instantaneous and conditionally averaged fields surrounding them. Section 3 discusses the transient growth of the velocity streaks and the primary flow dynamics therein, and the necessary condition of the sustainment of the dilatational TWP structures. Concluding remarks are given in § 4.

2. Kinematic depictions

2.1. *Numerical settings and flow parameters*

We consider a turbulent boundary layer at the free-stream Mach number $M_\infty = U_\infty/a_\infty = 5.84$ and the Reynolds number $Re_\infty = \rho_\infty U_\infty \delta_{in}/\mu_\infty = 32\,300$ over a flat plate with temperature $T_w = 1.77T_\infty = 0.25T_r$. Here, U_∞ and a_∞ are the free-stream velocity and sound speed, ρ_∞, T_∞ and μ_∞ are the free-stream density, temperature and viscosity, and δ_{in} is the nominal boundary layer thickness at the turbulent inlet. The recovery temperature T_r is the wall temperature with the adiabatic thermal boundary condition. The turbulence is governed by the Navier–Stokes equations of the compressible Newtonian perfect gas, written as

$$\frac{\partial \rho}{\partial t} + \frac{\partial \rho u_j}{\partial x_j} = 0, \tag{2.1}$$

$$\frac{\partial \rho u_i}{\partial t} + \frac{\partial \rho u_i u_j}{\partial x_j} = -\frac{\partial p}{\partial x_i} + \frac{\partial \tau_{ij}}{\partial x_j}, \tag{2.2}$$

$$\frac{\partial \rho E}{\partial t} + \frac{\partial \rho E u_j}{\partial x_j} = -\frac{\partial p u_j}{\partial x_j} + \frac{\partial \tau_{ij} u_i}{\partial x_j} - \frac{\partial q_j}{\partial x_j}, \tag{2.3}$$

with the following constitutive equation and Fourier's law of Newtonian flows to determine the viscous stress τ_{ij} and molecular heat conduction q_j as

$$\tau_{ij} = \mu\left(\frac{\partial u_i}{\partial x_j} + \frac{\partial u_i}{\partial x_j}\right) - \frac{2}{3}\mu\frac{\partial u_k}{\partial x_k}\delta_{ij}, \quad q_j = -\kappa\frac{\partial T}{\partial x_j}, \tag{2.4a,b}$$

and the state equation of the perfect gas as

$$p = \rho R T, \quad E = C_V T + \tfrac{1}{2}u_i u_i. \tag{2.5a,b}$$

The velocity component in the x_i direction ($i = 1, 2, 3$, also referred to as streamwise (x), wall-normal (y) and spanwise (z)) is denoted by u_i (or u, v and w). The density, pressure, temperature and total energy are represented by ρ, p, T and E, respectively. The dynamic viscosity μ is determined by Sutherland's law, and the heat conductivity as $\kappa = C_p\mu/Pr$, with R denoting the gas constant, C_p the specific heat per constant pressure, C_V the specific heat per constant volume, γ the ratio of specific heat, and Pr the molecular Prandtl number. The turbulent inlet is generated by the digital filtering technique proposed by Klein, Sadiki & Janicka (2003). At the wall, no-slip and no-penetration conditions and an isothermal condition for temperature are adopted. A periodic condition is utilized in the spanwise direction. No reflection conditions are enforced at the inlet, upper and outflow boundaries

so as to diminish the influences of numerical errors on the flow within the computational domain (Pirozzoli & Colonius 2013).

Other notations used in this paper are introduced as follows. The flow quantities normalized by the wall shear stress τ_w, density ρ_w and viscosity μ_w are marked by the superscript $+$. The friction Reynolds number $Re_\tau = \rho_w u_\tau \delta/\mu_w$ is approximately 450, with $u_\tau = \sqrt{\tau_w/\rho_w}$ the friction velocity. The ensemble average of a flow quantity is denoted by a bar, and the corresponding fluctuations by a prime. The density average is represented by a tilde, and the fluctuations by a double prime.

The DNS are carried out with OPENCFD-SC developed by Liang & Li (2013). A ninth-order upwind scheme and an eighth-order central scheme are adopted to approximate the convective and viscous terms, and the third-order TVD (total variation diminishing) Runge–Kutta scheme is utilized for time advancement.

The sizes of the computational domain in the three directions (L_x, L_y, L_z) are $(106, 9, 10)\delta_{in}$, discretized by $(3000, 330, 320)$ grids, respectively. The grids are distributed uniformly in the streamwise and spanwise directions with intervals $\Delta x^+ = 6.5$ and $\Delta z^+ = 5.7$, and stretched by a hyperbolic sine function in the wall-normal direction, with the first grid off the wall $\Delta y_w^+ = 0.7$ and the grid interval in the free-stream $\Delta y_\infty^+ \approx 9.6$. The simulation has been run for a time period of approximately $500\delta_{in}/U_\infty$ before the turbulence reaches a fully developed and statistically equilibrium state, and for another $500\delta_{in}/U_\infty$ to obtain the converged flow statistics. The results reported here are averaged in the spanwise and time directions, and also in the streamwise direction within the subdomain of $(70–90)\delta_{in}$.

In figure 1, we provide the wall-normal distribution of some basic flow statistics, compared with those reported by Zhang *et al.* (2018) with the same Mach number but a higher Reynolds number as a validation. Herein, the van Driest transformed mean velocity is calculated by the integration

$$u_{VD}^+ = \frac{1}{u_\tau}\int_0^{\tilde{u}} \sqrt{\frac{\bar{\rho}}{\bar{\rho}_w}}\,\mathrm{d}\tilde{u}. \tag{2.6}$$

The Reynolds stresses normalized by the mean wall shear stress τ_w is defined as

$$R_{ij}^+ = \frac{\overline{\rho u_i'' u_j''}}{\tau_w}. \tag{2.7}$$

The van Driest transformed mean velocity and mean temperature are shown in figures 1(*a*,*b*), along with the reference data. The Reynolds stresses shown in figure 1(*c*) conform reasonably well with those reported by Zhang *et al.* (2018) in the outer region (above $y \approx 0.4\delta$) but manifest consistent abatement in magnitudes for all components below $y \approx 0.3\delta$, which should probably be ascribed to the slightly lower Reynolds number in the present study. The root-mean-square (marked by the subscript '*rms*') of the vorticities ω_i' also show their consistency with the reference data, further validating the present DNS results. The velocity divergence ($\theta' = \partial u_i'/\partial x_i$), a direct indicator of compressibility effects, attains a maximum with magnitude of the same order as the vorticity at the wall, away from which it gradually decays to an insignificant level. This has been observed by some previous studies (Yu & Xu 2021; Baranwal, Donzis & Bowersox 2022), further consolidating the significance of compressibility effects in hypersonic turbulence over cold walls in the viscous sublayer.

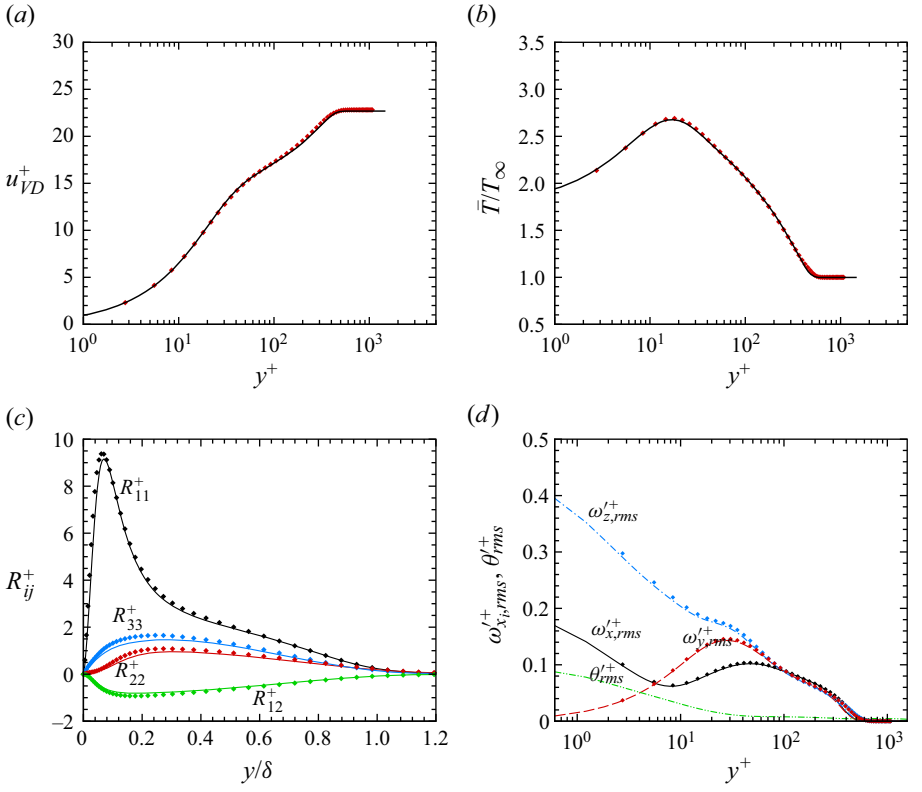

Figure 1. Wall-normal distributions of (*a*) u^+_{VD}, (*b*) $\bar{T}/T_\infty$, (*c*) R^+_{ij}, and (*d*) $\omega'^+_{x_i,rms}$ and θ'^+_{rms}. Lines indicate present DNS; symbols indicate results by Zhang, Duan & Choudhari (2018).

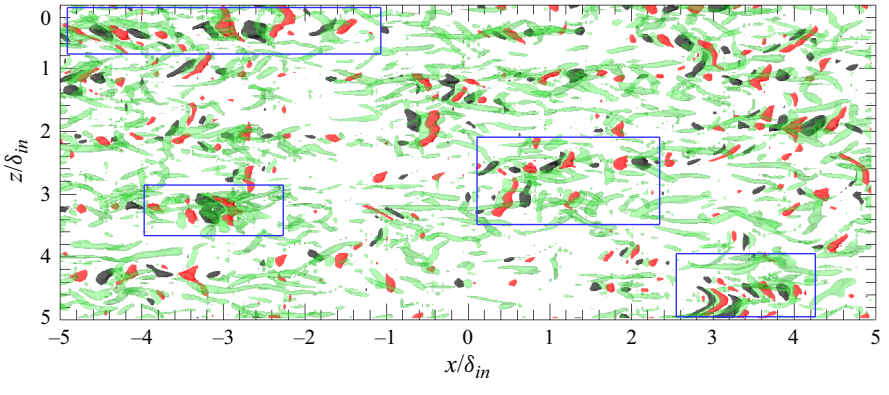

Figure 2. Top view of instantaneous fields $Q = 10$ (green), $\theta' = \pm 0.9$ (red positive, black negative).

2.2. *Instantaneous and averaged flow structures*

We first present the instantaneous distributions of the flow structures in hypersonic boundary layers over a cold wall as a direct impression of their organizations. Figure 2 displays the instantaneous distribution of dilatational and vortical structures. The former are visualized by the isosurfaces of positive and negative velocity divergence $\theta' = \partial u'_i/\partial x_i$, and the latter by those of the second invariant of the velocity gradient tensor Q.

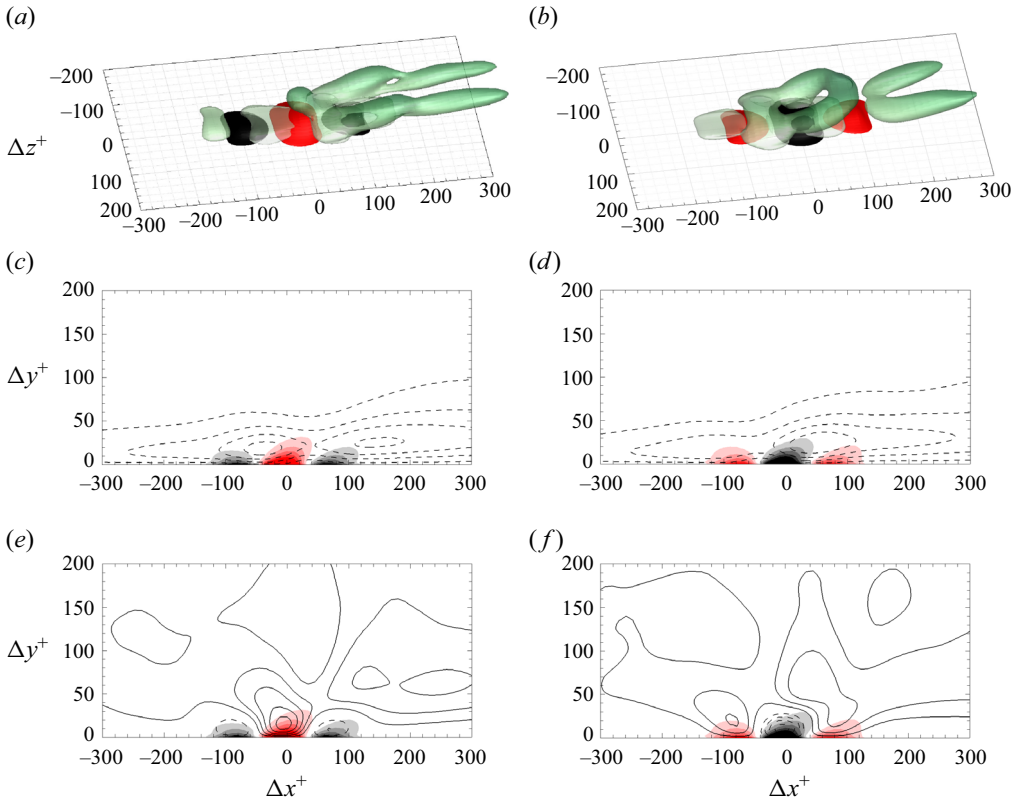

Figure 3. Averaged flow fields conditioned by $(a,c,e)\ \theta'(y^+ = 10) > \theta'_{rms}$ and $(b,d,f)\ \theta'(y^+ = 10) < -\theta'_{rms}$. (a,b) Isosurfaces of $\langle\lambda_{ci}\rangle = 0.4U_\infty/\delta_{in}$ (green) and $\langle\theta'\rangle = \pm 1.0U_\infty/\delta_{in}$ (red positive, black negative). $(c–f)$ The $\Delta z = 0$ plane, flooded with θ', lines: (c,d) $\langle u'\rangle$ $(-0.1 \sim +0.01 \sim 0.1)$ (the contour levels are set from -0.1 to $+0.1$ with the interval of 0.01), (e,f) $\langle v'\rangle$, $(-0.02 \sim +0.002 \sim 0.02)$, solid positive, dashed negative.

The morphology of these structures resembles those reported in the previous studies. The vortical motions align mainly in the streamwise direction in the near-wall region, as is observed commonly in canonical wall-bounded turbulence (Jiménez 2013). There also manifest vortices aligned in the spanwise direction close to the wall, corresponding to the stronger internal shear layer with the decreasing wall temperature (Yu & Xu 2021). The dilatational motions are organized as streamwise positive and negative alternating structures close to the wall, namely the TWP structures, as discovered by Yu *et al.* (2019) and Xu *et al.* (2021*a*) in hypersonic turbulent channels and boundary layers. These structures appear mostly beneath the comparatively strong vortical clusters, as highlighted by some boxes in figure 2. We can infer from their spatial association that the generation of the TWPs should probably be related to strong bursting events that are, in a sense, related to the clusters of vortices (Kim, Kline & Reynolds 1971; Robinson 1991; Tardu 1995; Adrian 2007; Hack & Schmidt 2021) incorporating sweeping and ejections.

A direct and intuitive inference of the generation of dilatational TWP structures is probably that ejections bring the fluid upwards, leading to the expansion of fluid elements, while sweeping events cause compression. This process is similar to the 'lift-up' process that forms low- and high-speed streaks. To verify this postulation, we present the averaged velocity and vortical structures surrounding the strong compressive and expansive events at $y^+ = 10$ in figures 3(*a*,*b*), denoted by $\langle\varphi\rangle$. They are obtained by performing ensemble

averaging of boxes whose centres satisfy the conditions $\theta' > \theta'_{rms}$ and $\theta' < -\theta'_{rms}$, respectively. As shown in figure 3(*a*,*b*), the vortical structures of the averaged flow field in the vicinity of the strong expansive events ($\theta'(y^+ = 10) > \theta'_{rms}$) close to the wall are organized as a reversed hairpin vortex with its head located close to the wall, whereas those under the condition of strong compressive events ($\theta'(y^+ = 10) < -\theta'_{rms}$) are organized as a hairpin vortex whose head is located at $y^+ \approx 50$. The legs of these vortices are connected with the quasi-streamwise vortices downstream (if the criteria are lowered) with the same rotational directions, bringing the low-speed fluid upwards. These hairpin vortices are usually representative of strong bursting events encompassing strong sweeps and ejections (Kim & Moin 1986; Adrian 2007).

The averaged streamwise and wall-normal velocities $\langle u' \rangle$ and $\langle v' \rangle$ at the centre plane $\Delta z^+ = 0$ are shown in figures 3(*c*–*f*). Surprisingly, whichever the event is, the strong dilatational motions are located beneath the streamwise elongated low-speed region, corresponding to the low-speed streaks in the instantaneous flow fields. The wall-normal velocity $\langle v' \rangle$ also shows some intriguing features. Expectedly, the expansive and compressive motions are related to the upward and downward vertical motions close to the wall, respectively. As it approaches further away from the wall ($y^+ \gtrsim 30$), the values of $\langle v' \rangle$ are positive for both cases, corresponding to ejections. This is in stark contrast to the intuitive depictions that expansive and compressive events are caused by ejections and sweeps, but consistent with the previous observations by Yu *et al.* (2019, 2022*b*), disproving that the sweeping and ejections, or equivalently the 'lift-up' processes, are responsible for the generation of dilatational TWP structures. Indeed, simple reasoning without reference to the governing equations often leads to paradoxical conclusions. Therefore, it is necessary to conduct detailed investigations in terms of flow dynamics.

3. Numerical experiments and flow dynamics

The proximity of dilatational TWP structures to the wall suggests that it is probably straightforward to investigate their dynamical association with the near-wall turbulent motions. It is well recognized that the near-wall turbulence can be regarded as the regeneration cycles between the velocity streaks and quasi-streamwise vortices (Hamilton, Kim & Waleffe 1995; Jiménez & Pinelli 1999; Schoppa & Hussain 2002; Jiménez 2013; Hwang & Bengana 2016). Such cycles can be summarized as (i) the amplification of the velocity streaks through the 'lift-up' effects of the streamwise vortices, (ii) the transient growth and/or the instability of the perturbations on the streaks, and (iii) the breakdown of streaks accompanied by the regeneration of the streamwise vortices. It seems that the velocity streaks are crucial in all the processes, and probably also in the generation of dilatational TWP structures. This is supported by the conditional averaged results in figures 3(*a*,*b*), which is consistent with the discovery of Yu *et al.* (2019) and Xu *et al.* (2021*a*) that dilatational motions tend to congregate beneath the low-speed streaks. This does not contradict the observations herein, for the bursting events that induce vortical clusters are usually related to the streak breakdown (Bogard & Tiederman 1986; Tardu 1995; Jiménez & Pinelli 1999), a fundamental process in the near-wall regeneration cycle.

3.1. *Transient growth on a steady streak*

Section 2 demonstrates that the formation of the dilatational TWP structures should be attributed, at least directly, not to the 'lift-up' effects, but probably to the streak breakdown. Such a process is initiated by the instability or transient growth of the streaks and will be the main focus of this subsection.

We consider the transient growth of two specific types of perturbations on temporally steady velocity streaks, namely those inducing the streak meandering and the dilatational TWP structures. For that purpose, we consider the two-dimensional base flow u_b as the superposition of the mean profiles and a streamwise and temporally invariant velocity streak $u_b(y,z) = \bar{u}(y) + u_s(y,z)$, where u_s is determined according to the morphology of the velocity streaks (Schoppa & Hussain 2002; Deng & Xu 2012)

$$u_s = A_s f(y)\cos(2\pi z/l_z), \quad f(y) = y/y_p \exp((1-y^2/y_p^2)/2), \tag{3.1a,b}$$

with amplitude $A_s = 6.4u_\tau$. The peak location and the spanwise width are set as $y_p^+ = 15$ and $l_z^+ \approx 180$ according to the peak of the premultiplied spanwise spectra of u' (Yu & Xu 2021) that represent the most intense location and the characteristic length scale of the velocity streaks, which are wider than those in incompressible turbulence. The density and temperature are set as their mean values $\bar{\rho}$ and $\bar{T}$ without incorporating initial perturbations. The perturbations inducing the streak meandering are initiated by the spanwise velocity

$$v'(t=0) = 0, \quad w'(t=0) = A_w f(y)\sin(2\pi k_x x/l_x), \tag{3.2a,b}$$

referred to as case LW (abbreviation for 'linear w' perturbation'), and those inducing the dilatational TWPs by the wall-normal velocity

$$v'(t=0) = A_v f(2y)\sin(2\pi k_x x/l_x), \quad w'(t=0) = 0, \tag{3.3a,b}$$

referred to as case LV (abbreviation for 'linear v' perturbation'). Transient growth simulations with the fixed base flow are performed with the streamwise and spanwise periodic conditions to obtain the temporal evolution of these two types of perturbations. The streamwise and spanwise sizes of the computational domain are set to be $l_x^+ = 2000$ and $l_z^+ \approx 180$, respectively. A series of streamwise wavenumbers with $k_x = 1 \sim 8$ for case LW and $k_x = 7 \sim 14$ for case LV are considered, covering the streamwise length scales of the quasi-streamwise vortices and the dilatational TWP structures (Yu & Xu 2021; Huang *et al.* 2022). The initial amplitude of the perturbation is set as $A_w = A_v \approx 0.25u_\tau \approx 0.01U_\infty$.

The amplification rates of the volume-averaged turbulent kinetic energy E_k of the perturbations, defined as $G(t) = E_k(t)/E_k(0)$, are shown in figure 4(*a*). For case LW with $k_x = 4$, the w' perturbations are amplified monotonically and reach such high levels that the nonlinear effects cannot be disregarded. After the initial transient growth, $G(t)$ increases exponentially, suggesting that the instability of the low-speed streak at this strength when perturbed by the streamwise alternating w' leads to its meandering. The instantaneous flow field at $t^+ = 250$ in figure 4(*c*) shows that the streaks are 'pushed over' and the quasi-streamwise vortices are generated, consistent with the phenomena in incompressible flows (Schoppa & Hussain 2002; Xu *et al.* 2013; Wang, Huang & Xu 2015; Jiménez 2018). The dilatational structures in this case are much weaker and follow the patterns of the vortices, but no feature of the TWPs can be observed. Similar conclusions can be obtained for other streamwise wavenumber cases with $k_x = 1$–8 (grey lines in figure 4*a*), amongst which the perturbations with $k_x = 4$ are the most unstable or the least stable.

Regarding case LV, the v' perturbations with $k_x = 10$ are capable of triggering the dilatational TWP structures (figure 4*d*). However, the amplification rate $G(t)$ keeps decreasing, despite its resemblance to the Mack mode (second mode) that is the least stable and triggers the transition of hypersonic laminar boundary layers (Fedorov 2011; Sharma & Girimaji 2023), thereby excluding the emergence of dilatational TWPs being

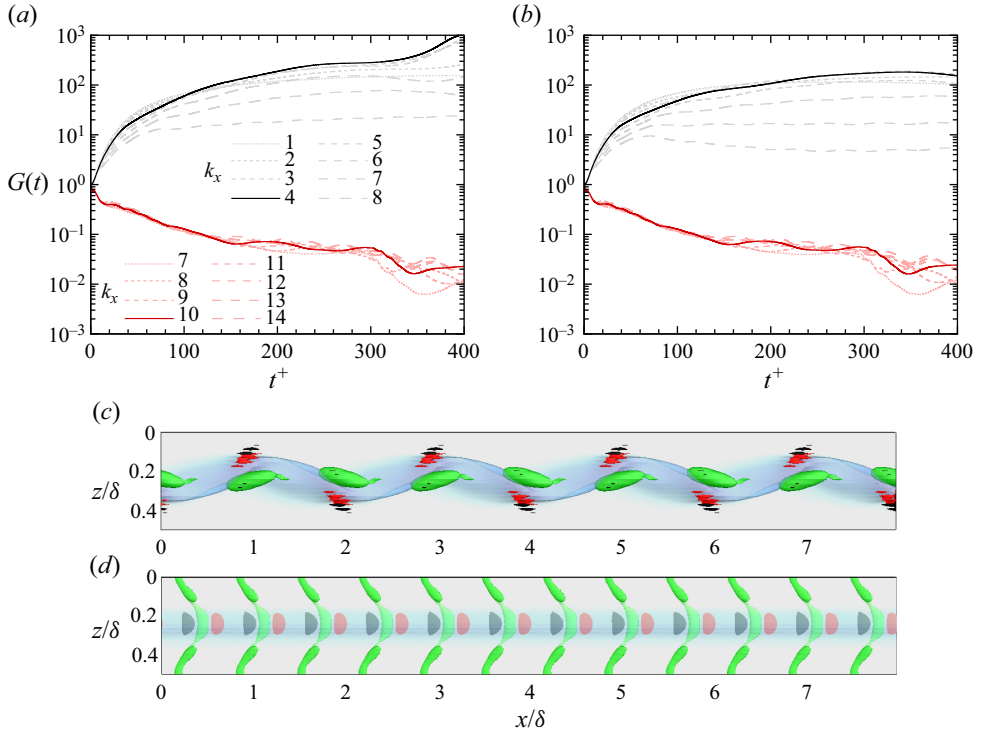

Figure 4. (*a*,*b*) Linear transient growth of perturbations $G(t)$ (black and grey, cases LW; red and light red, cases LV) (*a*) with and (*b*) without the density and temperature streaky structures as the base flow. (*c*,*d*) Flow structures at $t^+ = 200$, isosurfaces of Q (green), $u^+ = 6$ (translucent blue) and θ' (red positive, black negative) for (*c*) case LW, $Q = 2$, $\theta' = \pm 0.25$, and (*d*) case LV, $Q = 0.2$, $\theta' = \pm 0.4$.

its inherent instability or the transient growth of the acoustic modes (Zhang *et al.* 2022). The results are qualitatively the same if the streamwise wavenumber k_x is set within the range $k_x = 7$–14 (light red dashed lines in figure 4*a*). Based on the observations above, we conclude that the transient growth of linear perturbations – either the spanwise or the wall-normal velocity – on the velocity streaks is not responsible for the generation of the dilatational TWP structures.

The discussions above did not incorporate the thermodynamic flow quantities in the two-dimensional base flows. It is well known that the streamwise velocity fluctuations are highly correlated with the density and temperature fluctuations (Zhang *et al.* 2014), both organized as the streamwise elongated streaks in the near-wall region (Pirozzoli & Bernardini 2011). It is possible that these flow quantities influence the processes of the perturbation amplification. Henceforth, we consider the streaks of the temperature and the density streaks in the two-dimensional base flow as

$$T_s = \frac{\partial \bar{T}}{\partial \bar{u}}\, u_s, \quad \rho_s = -\frac{\bar{\rho}}{\bar{T}} T_s. \tag{3.4a,b}$$

The temporal evolutions of $G(t)$ under such base flows are shown in figure 4(*b*). Compared with figure 4(*a*), it appears that the perturbation amplifications are less intense when the temperature and density streaks are involved, suggesting that the velocity streaks accompanied by the density and viscosity stratifications are more stable. Nevertheless, the conclusions are qualitatively the same as those obtained previously, that

the w' perturbations are capable of intensifying via the transient growth, while the v' perturbations can only decay monotonically, showing no evidence of triggering higher magnitudes of perturbations.

We note that the TWPs and the Mack modes in hypersonic turbulent boundary layer transition share many similar features. For example, (i) they share the same morphology, behaving as the travelling waves with a certain wavenumber, (ii) they are both located close to the wall, (iii) the TWPs are intensified by the rising Mach number and the cooling wall (Yu *et al.* 2019; Unnikrishnan & Gaitonde 2021; Yu & Xu 2021), and the second mode is destabilized by these factors (Mack 1984; Stetson & Kimmel 1992), and (iv) they can both enhance the wall pressure fluctuations (Casper, Beresh & Schneider 2014; Yu *et al.* 2020; Unnikrishnan & Gaitonde 2021). It is probably the different base flows that lead to the disparity in the growth of these perturbations. Rigorous proof is needed to conclude that the Mack modes and the TWPs are the same type of coherent structures, which is beyond the scope of the present study.

3.2. *Flow dynamics in a regeneration cycle*

We further discuss the evolution and breakdown of the velocity streaks. We perform numerical simulations (named as case NW, short for 'nonlinear w' perturbation') similar to case LW in § 3.1, with the exception that the base flow is set as the mean profiles $\bar{u}$, $\bar{\rho}$ and $\bar{T}$, and enforced to be steady, thereby allowing the meandering and breakdown of the velocity streaks. The initial perturbations are the superposition of the velocity streaks and the streamwise alternating spanwise velocity

$$\left.\begin{aligned} u'(t=0) &= A_s f(y)\cos(2\pi k_z z/l_z),\\ v'(t=0) &= 0,\\ w'(t=0) &= A_w f(y)\sin(2\pi k_x x/l_x), \end{aligned}\right\} \tag{3.5}$$

with k_z being the spanwise wavenumber. The streamwise length of the domain is set as $l_x^+ = 2000$, the streamwise wavenumber of the perturbation as $k_x = 4$, the spanwise width as $l_z^+ = 360$, and the spanwise wavenumber as $k_z = 2$, containing two velocity streaks in the spanwise direction (Yu & Xu 2021). The amplitudes of the streaks and the spanwise velocity are $A_s = 6.4u_\tau$ and $A_w = 1.2u_\tau$ so that the intensities of the perturbations are the same as the DNS results at $y^+ = 15$. Such an initial perturbation field is divergence-free, so the dilatational motions shown later are generated by flow dynamics instead of being initially introduced artificially. The reason for using a wider domain will be explained later.

Figure 5(*a*) shows the temporal evolution of E_k below $y^+ = 60$, which is split as two portions E_{ks} and E_{kw}. The former is defined as

$$E_{ks}(t) = \frac{1}{l_x l_z \delta}\int_0^{l_z}\int_0^{y^+=50}\int_0^{l_x}\frac{1}{2}\langle\rho\rangle_x\langle u''\rangle_x^2\,\mathrm{d}x\,\mathrm{d}y\,\mathrm{d}z, \tag{3.6}$$

with $\langle\cdot\rangle_x$ being the streamwise average, representing the energy of the streamwise elongated straight streaks; the latter is $E_{kw}(t) = E_k(t) - E_{ks}(t)$, the energy of wavy structures (Doohan, Willis & Hwang 2021). Figure 5(*b*) displays the temporal evolution of vortical enstrophy ϵ_ω^+ (the volume-averaged intensity of turbulent vorticity vector $|\omega_i|^2$) and the dilatational enstrophy ϵ_θ^+ (the volume-averaged intensity of velocity divergence θ'^2). The initially introduced velocity streaks gradually decay while the wavy structures amplify, with E_{ks} attaining local minimum and E_{kw} local maximum at t_1^+. At this time instant, the meandering of the streaks and the quasi-streamwise vortices are the most

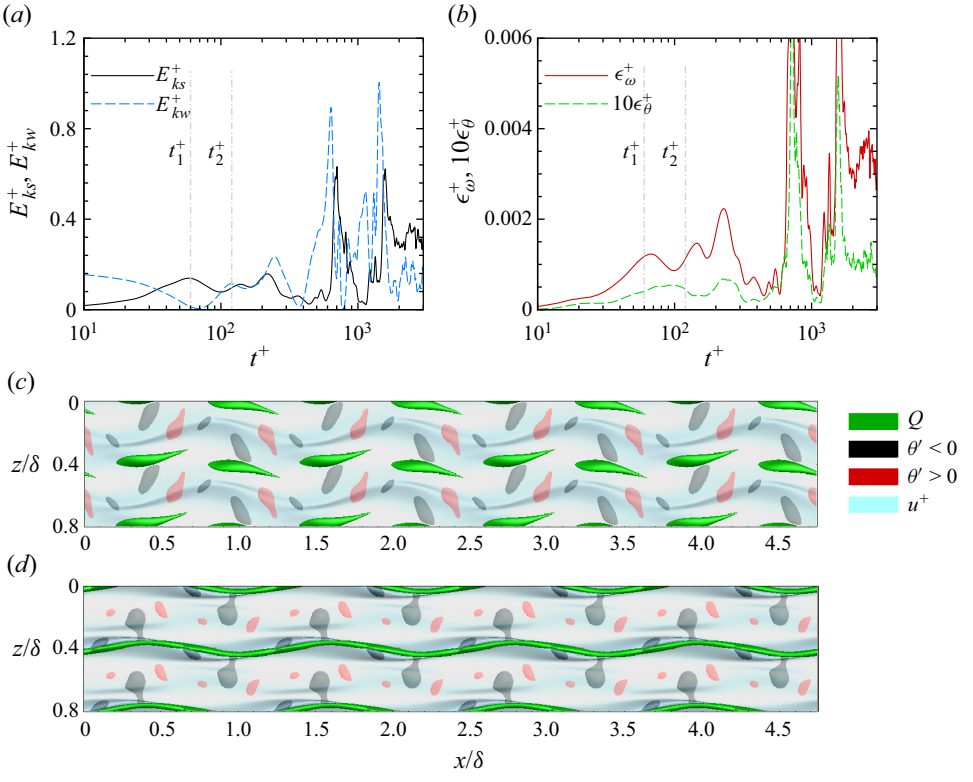

Figure 5. Temporal evolution of (*a*) E_{ks} and E_{kw}, (*b*) ϵ^+_ω and ϵ^+_θ in case NW. (*c*,*d*) Instantaneous flow fields at t_1 and t_2, with the isosurfaces $u^+ = 13$, $Q = 1.4$ and (*c*) $\theta' = \pm 0.7$, (*d*) $\theta' = \pm 0.35$.

intense, as shown in figure 5(*c*). As the perturbations continue to evolve, E_{ks} increases and E_{kw} decreases, reminiscent of the regeneration/reamplification of the streamwise elongated streaks rolled up by the quasi-streamwise vortices (Xu *et al.* 2013; Hwang & Bengana 2016). At t^+_2, the former reaches a local maximum and the latter a local minimum, and they retain nearly constant value for a time period of approximately $10\delta_v/u_\tau$. During this time, the vortical enstrophy ϵ^+_ω continues to increase while the dilatational enstrophy ϵ^+_θ starts to decrease. The instantaneous field at t^+_2 in figure 5(*d*) shows that the velocity streaks are less meandering, the vortices are more streamwise-aligned, and the dilatational structures are weakened, compared to those at t^+_1.

Notably, it can be observed that a pair of dilatational structures is manifested below each streamwise vortex in this case, manifesting a shape similar to that of the TWPs. This is in stark contrast to the flow organizations in case LW, where the velocity streak is enforced as the steady base flow and the perturbations are weak. The only reasonable explanation for this phenomenon is the comparatively strong nonlinearity in the process of streak meandering and breakdown, which triggers the generation of dilatational TWP structures. This inference is supported by the fact that there are eight pairs of dilatational structures but only four pairs of streamwise vortices, the latter of which is consistent with the k_x of the initial perturbation. These dilatational structures should be triggered by the second harmonic via nonlinear effects, the triad-wave interactions being the most probable mechanism.

Significant physical insights can be gained upon an inspection of the governing equations for velocity divergence and its approximation in the viscous sublayer. By taking the divergence of the momentum equation in its non-conservative form

$$\frac{\partial u_i}{\partial t} + u_j \frac{\partial u_i}{\partial x_j} = -\frac{1}{\rho}\frac{\partial p}{\partial x_i} + \frac{1}{\rho}\frac{\partial \tau_{ij}}{\partial x_j}, \tag{3.7}$$

we obtain the following transport equation of the velocity divergence θ, or θ' due to the lack of mean flow dilatation herein:

$$\frac{\mathrm{D}\theta}{\mathrm{D}t} = -\frac{\partial u_i}{\partial x_j}\frac{\partial u_j}{\partial x_i} - \frac{1}{\rho}\frac{\partial^2 p}{\partial x_j \partial x_j} + \frac{1}{\rho^2}\frac{\partial \rho}{\partial x_j}\frac{\partial p}{\partial x_j} + \frac{\partial}{\partial x_i}\left(\frac{1}{\rho}\frac{\partial \tau_{ij}}{\partial x_j}\right). \tag{3.8}$$

By applying the zeroth-order near-wall approximations of the no-slip and isothermal conditions $u_i \approx O(y)$ and $T \approx T_w(1 + O(y))$ to the continuity equation and the state equation, we have $\theta \approx -(1/\rho)\,\partial\rho/\partial t$ and $p = \rho R T_w$, and the following correlation between the temporal derivative of θ and pressure p:

$$\frac{\partial \theta}{\partial t} \approx \frac{1}{\rho^2}\left(\frac{\partial \rho}{\partial t}\right)^2 - \frac{1}{\rho}\frac{\partial^2 \rho}{\partial t^2} \approx \theta^2 - \frac{1}{\rho}\frac{\partial^2 \rho}{\partial t^2} \approx \theta^2 - \frac{1}{p}\frac{\partial^2 p}{\partial t^2}. \tag{3.9}$$

The third term on the right-hand side of (3.8) can be simplified as

$$\frac{1}{\rho^2}\frac{\partial \rho}{\partial x_j}\frac{\partial p}{\partial x_j} \approx \frac{1}{\rho^2}\frac{\partial \rho'}{\partial x_j}\frac{\partial p'}{\partial x_j} \approx \frac{1}{R T_w}\left(\frac{1}{\rho}\frac{\partial p'}{\partial x_j}\right)\left(\frac{1}{\rho}\frac{\partial p'}{\partial x_j}\right), \tag{3.10}$$

by presuming the insignificance of the wall-normal derivative $\partial p'/\partial x_2 \approx 0$. Equation (3.8) can thus be rewritten in the form of wave propagation

$$-\frac{\gamma}{a^2}\frac{\partial^2 p}{\partial t^2} + \frac{\partial^2 p}{\partial x_j \partial x_j} \approx -2\rho Q + \frac{1}{\rho R T_w}\frac{\partial p'}{\partial x_j}\frac{\partial p'}{\partial x_j} + \rho\frac{\partial}{\partial x_i}\left(\frac{1}{\rho}\frac{\partial \tau_{ij}}{\partial x_j}\right), \tag{3.11}$$

where a is the sound speed. Note that this reformulation of the governing equation does not indicate that the wall pressure propagates as a sound wave within the wall-parallel plane. Rather, it suggests that the pressure Laplacian term balances, at least partially, the temporal derivative.

We still focus on (3.8) and will give reference to (3.11) when necessary. The right-hand-side terms of (3.8) at t_1^+ are shown in figure 6. The first term on the right-hand side of (3.8) (referred to as S_{VG}, figure 6*a*) represents the contribution of the velocity gradient. This term is strong off the wall from the buffer layer and is related to the second invariant of the velocity gradient Q ($S_{VG} = \theta^2 - 2Q$) and the self-induced nonlinear generation term θ^2, the latter of which cannot be excited by itself if no initial velocity divergence is introduced. Since the velocity divergence θ is much weaker than vorticity and shear above the viscous sublayer (Yu & Xu 2021), S_{VG} is approximately equal to Q. Given its different spatial distributions from those of the dilatational structures, and the fact that this term also exists in incompressible turbulence, the generation of the dilatational structures cannot be attributed to this term. The last term on the right-hand side of (3.8) (S_{VD}, figure 6*b*) originates from the viscous term, interpreted as viscous dissipation. Like the S_{VG} term, it also exists in incompressible flows and is unrelated to the Mach number. Henceforth, it cannot be related directly to the effects of compressibility and thereby the formation of dilatational TWP structures, despite their resemblance.

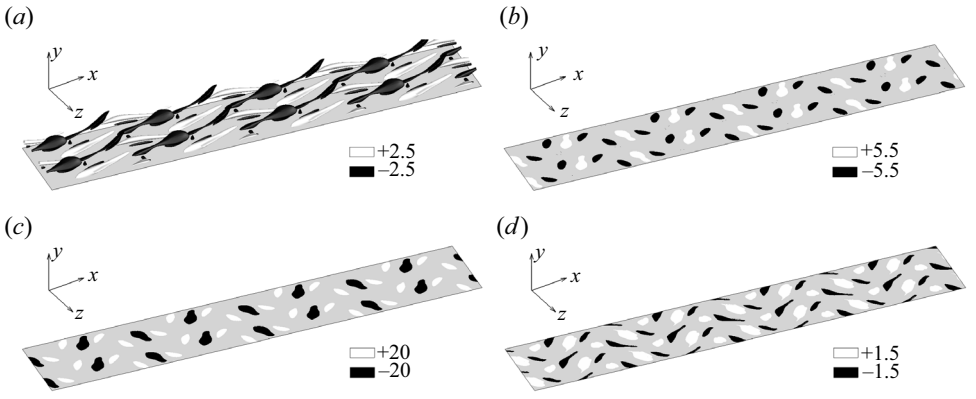

Figure 6. Instantaneous distributions of the right-hand side of (3.8) at t_1^+: (*a*) S_{VG}, (*b*) S_{VD}, (*c*) S_{PL}, and (*d*) S_{PB}.

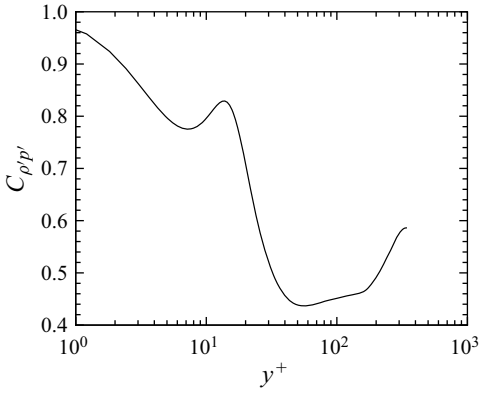

Figure 7. Correlation coefficient $C_{\rho'p'}$ between ρ' and p'.

The two remaining terms on the right-hand side of (3.8) are related to pressure, a flow quantity that is linked to both dynamic and thermodynamic flow quantities. These two terms arise from the pressure Laplacian (S_{PL}, figure 6*c*) and the barotropic effects (S_{PB}, figure 6*d*), respectively, the latter of which is caused by the parallel density and pressure gradient. Although the S_{PL} term is strong, it functions primarily as the propagation effects and balances the temporal derivative, as demonstrated by (3.11). The S_{PB} term is worth exploring. When normalized by ρ_∞, U_∞ and the free-stream temperature T_∞, the coefficient $1/(RT_w)$ in the S_{PB} term (see (3.10)) can be non-dimensionalized to be $\gamma M_\infty^2/T_w$. This suggests that the S_{PB} term will be enhanced by the increasing Mach number and the decreasing wall temperature, which is consistent with the evidence given by previous studies (Yu *et al.* 2019, 2020; Yu & Xu 2021; Zhang *et al.* 2022). We should point out that one of the important postulations of $p' \propto \rho'$, or equivalently $C_{\rho'p'} \approx 1$, can be satisfied only within the viscous sublayer due to the isothermal condition (see figure 7). It fails rapidly off the wall, where the gradients of density and pressure fluctuations $\nabla\rho'$ and $\nabla p'$ are no longer parallel to each other, resulting in the trivial contribution from the S_{PB} term. This also explains why the dilatational motions are significant only in the viscous sublayer. Furthermore, the S_{PB} term is a nonlinear expression that is capable of triggering higher harmonics. Specifically, for the pressure fluctuations with a certain streamwise

wavenumber k_x and angular frequency ω in the form of a travelling wave, say $p_{k_x,\omega} = \hat{p}(-k_x x + \omega t)$, the S_{PB} term is capable of triggering the fluctuations at the streamwise wavenumber at $2k_x$, then at $4k_x$, $8k_x$, and so on, to the extent that the nonlinearity is strong enough, until the very small scales where the viscous dissipation overwhelms the other mechanisms of their generation, with the most evident structures manifested at the scale where the production balances the dissipation. These descriptions regarding the generation of pressure p' can be related to θ' by the approximation $\theta' \approx -(1/p)\,\partial p'/\partial t$. It is therefore justifiable to attribute the generation of the dilatational TWP structures to the S_{PB} term, caused by the restriction of the isothermal boundary condition, and hence the parallel gradients of pressure and density.

Notably, the primordial wall pressure fluctuations (prior to the emergence of TWPs) are generated by the vortical structures that are associated with solenoidal turbulent motions in the buffer region. There is no direct evidence that the wall pressure fluctuations related to the dilatational TWP structures are self-induced, self-sustained or accountable for perturbation amplification or the generation of unstable vortical motions, as has been proven in the previous subsection.

3.3. *Analysis of the fully turbulent regime*

The previous discussion explain why the dilatational motions are the most intense in close proximity to the wall instead of at higher wall-normal locations, and how the TWP structures are generated through the already existing wall pressure fluctuations. However, this is not sufficient to support the conclusion that the dilatational motions are generated by the nonlinearity of the streak meandering in the regeneration cycle, because this assertion implies that the spanwise characteristic length scales of the TWP structures and the low-speed streaks should be approximately the same, which is not the case. As we have shown in our previous study (Yu *et al.* 2019, 2020), the spanwise characteristic length scales of pressure p' and flow divergence θ' are 2–3 times that of the velocity streaks in the buffer region, indicating that there probably exist subharmonic excitations of the fluctuations. This is more challenging to interpret physically than the shorter streamwise length scales, for the fluctuations at lower wavenumbers (larger characteristic length scale) can be excited only at the last stage of transition (as will be shown later). Directly tracing causality from the instantaneous fields is an arduous and potentially futile task, given the complexity of flow dynamics in the strong nonlinear stage of flow transition or fully developed turbulence. However, scrutinizing the evolution of coherent structures by prohibiting certain effects will shed some interesting light on flow physics.

We perform two additional simulations by setting the spanwise width of the computational domain as $l_z^+ \approx 180$ and 540, and spanwise wavenumber $k_z = 1$ and 3 (in (3.5)), referred to as cases NWn (case NW in a narrower domain) and NWw (case NW in a wider domain), respectively, in order to reveal the impact of motions with spanwise scales wider than the near-wall velocity streaks on the structural variation of the near-wall dilatational motions. Figure 8 shows the temporal evolution of E_k^+ and ϵ_θ^+ within $y^+ = 60$. From the initial state $t^+ = 0$ to $t^+ = 1300$, during which the flows have gone through several low-intensity and one high-intensity bursting events, the turbulent kinetic energy E_k^+ and dilatational enstrophy ϵ_θ^+ of the three cases are almost identical, indicating that the turbulent motions can be considered to evolve as independent clusters with the same streamwise and spanwise length scales as the initially introduced perturbations without significant nonlinear effects to trigger larger-scale motions, at least in the spanwise direction where the sizes of the computational domain differ in these cases. Within this

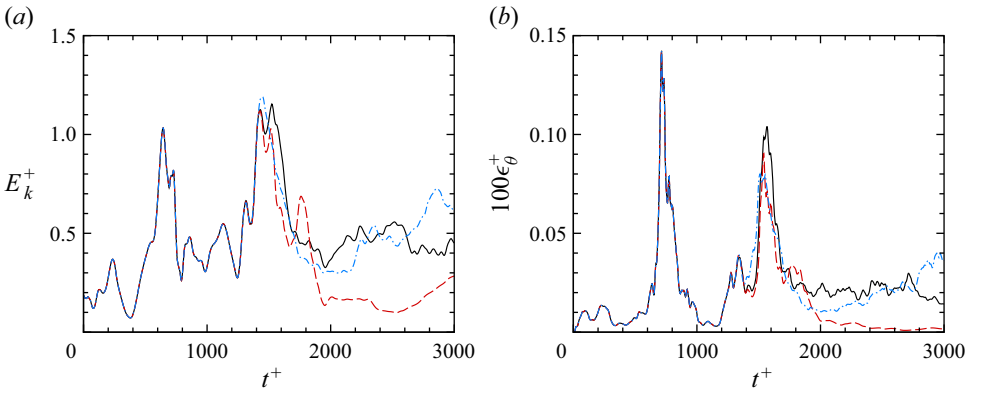

Figure 8. Temporal evolution of (*a*) E_k and (*b*) ϵ_θ^+. Red dashed lines, case NWn; black solid lines, case NW; and blue dash-dotted lines, case NWw.

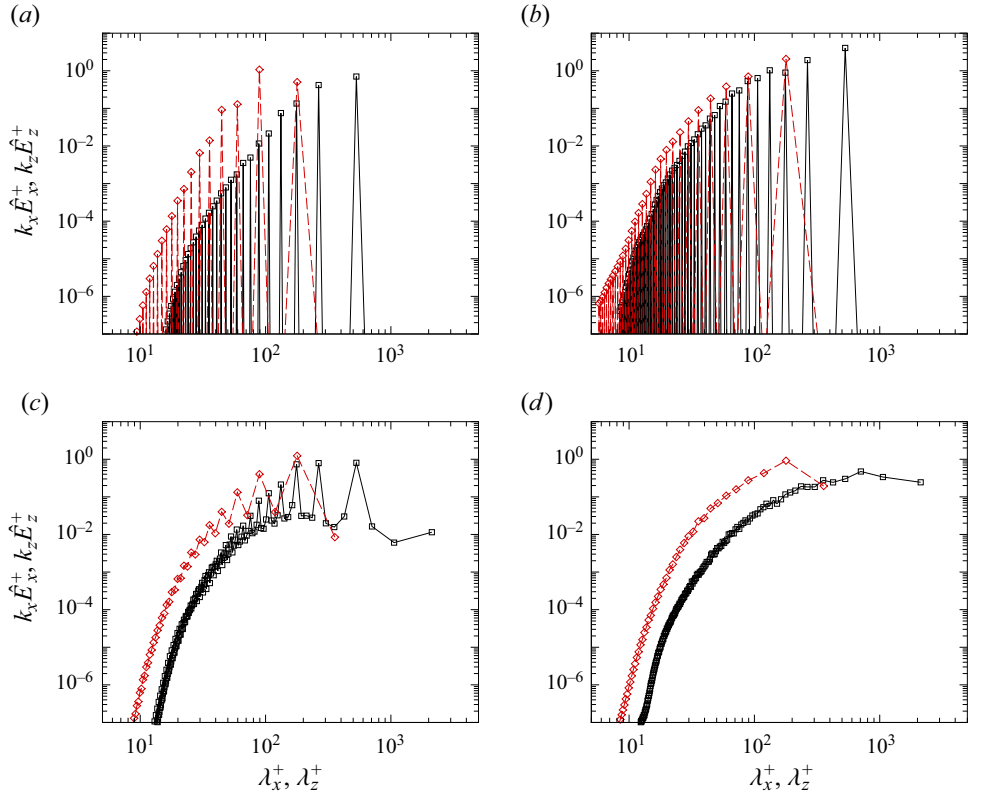

Figure 9. Premultiplied streamwise (black solid lines) and spanwise (red dashed lines) spectra integrated below $y^+ = 60$ at three peaks of E_k: (*a*) $t^+ = 250$, (*b*) $t^+ = 640$, (*c*) $t^+ = 1350$, (*d*) $t^+ = 1720$.

period, the spanwise spectra remain discrete, which is a typical phenomenon in transition flows, as shown in figures 9(*a*,*b*). It can also be inferred from the instantaneous flow fields in figures 10(*a*,*b*) that the structures are still periodic, organized as clusters with the sizes of the initially introduced wavelengths. From $t^+ \approx 1300$, E_k^+ and ϵ_θ^+ commence to diverge after reaching very high peak values, corresponding to a highly intensified

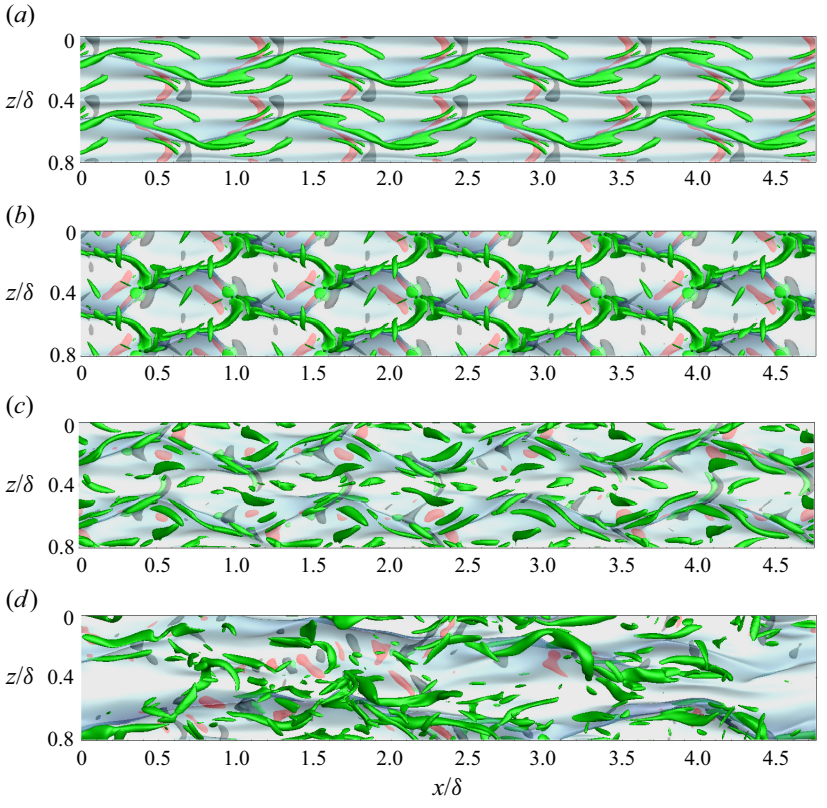

Figure 10. Instantaneous distribution of vortices (isosurfaces of λ_{ci}, green), dilatational motions (θ', black and red) and velocity streaks ($u^+ = 13$, translucent blue) for (*a*) $t^+ = 250$ ($Q = 1.2$, $\theta' = \pm 0.7$), (*b*) $t^+ = 640$ ($Q = 6$, $\theta' = \pm 3$), (*c*) $t^+ = 1350$ ($Q = 2.5$, $\theta' = \pm 2.5$), and (*d*) $t^+ = 1720$ ($Q = 2.5$, $\theta' = \pm 2.5$).

turbulent bursting event. After that, both of these flow quantities diminish to comparatively lower levels around which they oscillate. It is not until this second strong bursting event that the spanwise spectra gradually become continuous, as displayed in figures 9(*c*,*d*), and the initially introduced periodicity vanishes completely, accompanied by the amplified energy at scales greater than those of the streaks. By comparison, E_k^+ and ϵ_θ^+ in case NWn are evidently lower than those in the other two cases. Considering that the 'healthy' turbulent height is approximately one-third of the spanwise width of the computational domain (Flores & Jiménez 2010; Yin, Huang & Xu 2017), the lower turbulent kinetic energy E_k^+ in case NWn can be ascribed to the diminished turbulent fluctuations near and above the healthy turbulence height $y^+ \approx 60$. The abatement of ϵ_θ^+, however, cannot be explained similarly, for the strong velocity divergence is restricted within the viscous sublayer and cannot reach such a high off-wall distance. Instead, it is more rational to associate the 'healthy' dilatational TWP structures, those endowed with the features of the same structures in regular turbulent boundary layers in larger computational sizes, with the strong turbulent fluctuations at larger scales and higher locations, the lack of which directly influences their generation.

We would like to comment on the small-scale spanwise-oriented vortical structures located within and slightly above the dilatational TWP structures, which are clearly visible in fully-developed turbulence in figure 2. However, these structures can be barely observed during the initial stage of the transient growth, suggesting that their formation occurs

during subsequent processes. Their correlation with the dilatational motions (Yu *et al.* 2022*b*) can be explained by simple reasoning. The dilatational motions are correlated with the strong wall-normal velocity v' close to the wall. As they are organized as streamwise positive–negative alternating structures, the strong $\partial v/\partial x$ should be expected. Additionally, the wall-normal velocity brings the low-speed fluids upwards and high-speed fluids downwards, similar to the streamwise vortices in the buffer region, inducing $\partial u'/\partial y$. Both of these processes are related to the spanwise vorticity ω_z'. Such a description interprets the process of the dilatational motions generating solenoidal vortical ones. But then again, these spanwise vortices lack the mechanisms of self-sustainment, so the initial dilatational disturbances cannot trigger the transition, as proved in § 3.1.

3.4. *Correlation with the Orr mechanism*

The vortical clusters are found to be associated with turbulent bursting events (Kim & Moin 1986; Tardu 1995; Adrian 2007). It has been proven that the vortical clusters are related to the Orr mechanism (Encinar & Jiménez 2020; Jiao, Hwang & Chernyshenko 2021; Lozano-Durán *et al.* 2021), which describes the velocity and pressure perturbation amplification during their variation from the backward tilting to the forward tilting structures in the flows with mean shear (Orr 1907). Lozano-Durán *et al.* (2021) conducted numerical experiments in which the Orr-mechanism-related pressure fluctuations in the wall-normal momentum equation are removed, and found that the near-wall turbulence is laminarized. This suggests the significant role played by the Orr mechanism in the near-wall turbulence. In light of this, we also attempt to mitigate the Orr mechanism, and hence the turbulent bursts and vortical clusters, for the purpose of investigating their influences on the dilatational TWP structures.

Lozano-Durán *et al.* (2021) pointed out that the Orr mechanism contributes mainly to the slow term of the pressure fluctuations, inhibiting the cross-shear velocities when the structures are tilted. Presuming that such a conclusion is also valid in compressible turbulence, we propose to cast the wall-normal momentum equation as follows to alleviate the Orr mechanism:

$$\frac{\partial \rho v}{\partial t} + \frac{\partial \rho u_j v}{\partial x_j} = -\frac{\partial p}{\partial y} + \frac{\partial \tau_{2j}}{\partial x_j} + \alpha \frac{\partial p_s'}{\partial y}. \tag{3.12}$$

Here, the slow term p_s' is solved by the Poisson equation

$$\frac{\partial^2 p_s'}{\partial x_i \partial x_i} = -\frac{\partial^2}{\partial x_i \partial x_i}(\rho u_i'' u_j'' - \overline{\rho u_i'' u_j''}), \tag{3.13}$$

with the boundary conditions $\partial p_s'/\partial y = 0$ on the wall and $p_s' = 0$ at the upper boundary, following the study of Zhang *et al.* (2022). When taking the parameter $\alpha = 1.0$, the slow term will be eliminated. In our simulation, we set α as 0.5 and 0.8 to remove the slow term partially for the consideration of numerical stability, and as 0.0 for comparison.

We commence our simulations from a fully developed flow field at $t^+ = 3000$ in case NW. The cases with various α have been run for a period $1000\delta_v/u_\tau$. The temporal evolution of the divergence fluctuation intensity at the wall is shown in figure 11. Compared with the case with $\alpha = 0$, the θ_{rms}' values on the wall are significantly lowered as the values of α increase, especially the high rising peaks indicating the occurrence of strong turbulent bursting events, suggesting the weakening of the dilatational motions with the alleviation of the Orr mechanism. By observing the instantaneous flow fields in figure 12, we found that removing the slow term of the pressure that is closely related to

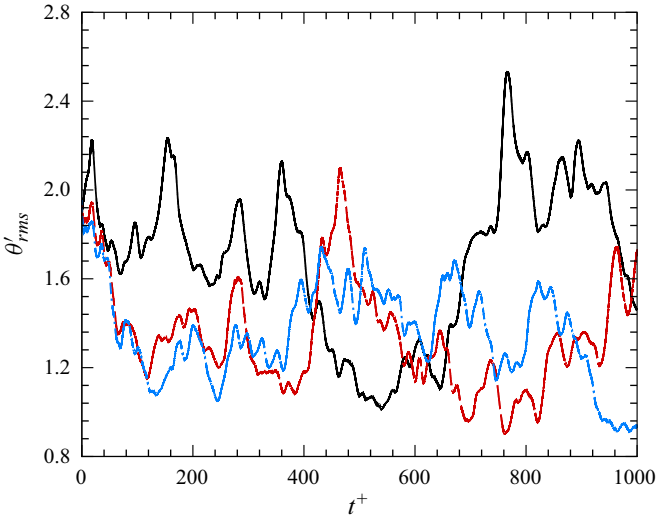

Figure 11. Evolution of θ'_{rms} on the wall: black solid line, $\alpha = 0$; red dashed line, $\alpha = 0.5$; blue dash-dotted line, $\alpha = 0.8$.

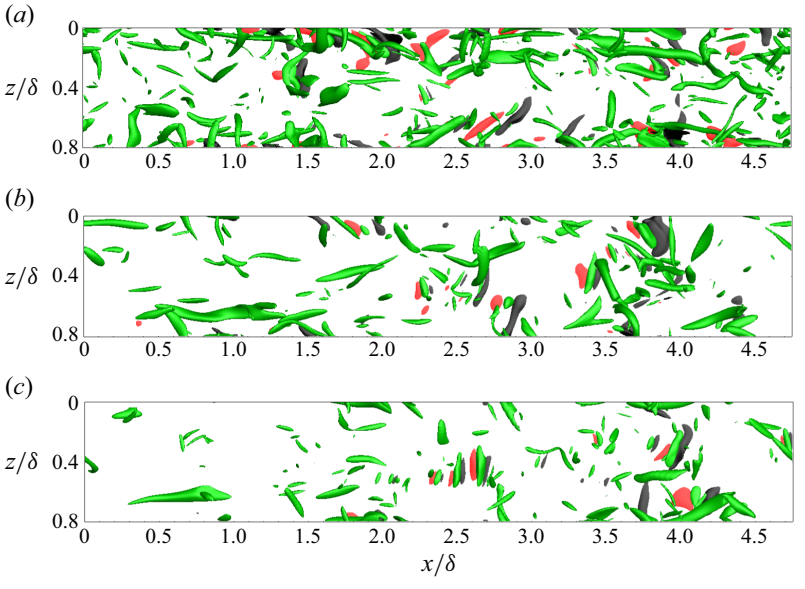

Figure 12. Instantaneous distribution of vortices (isosurfaces of $Q = 2.5$, green) and dilatational motions ($\theta' = \pm 2.5$, black and red) at $t^+ = 100$ for (*a*) $\alpha = 0$, (*b*) $\alpha = 0.5$, and (*c*) $\alpha = 0.8$.

the Orr mechanism leads to the evident weakening of the vortical structures, accompanied by the diminishing dilatational TWP structure beneath them.

However, we must point out that the simple numerical experiment conducted herein constrained the nonlinearity more than the Orr mechanism. It remains unclear whether the Orr mechanism or the other nonlinear effects should be attributed to the generation or the sustainment of the dilatational TWP structures. Such ambiguity does not affect our conclusion that the vortical clusters and dilatational TWP structures occur simultaneously in hypersonic wall turbulence, and that the vortical clusters related to the bursting events

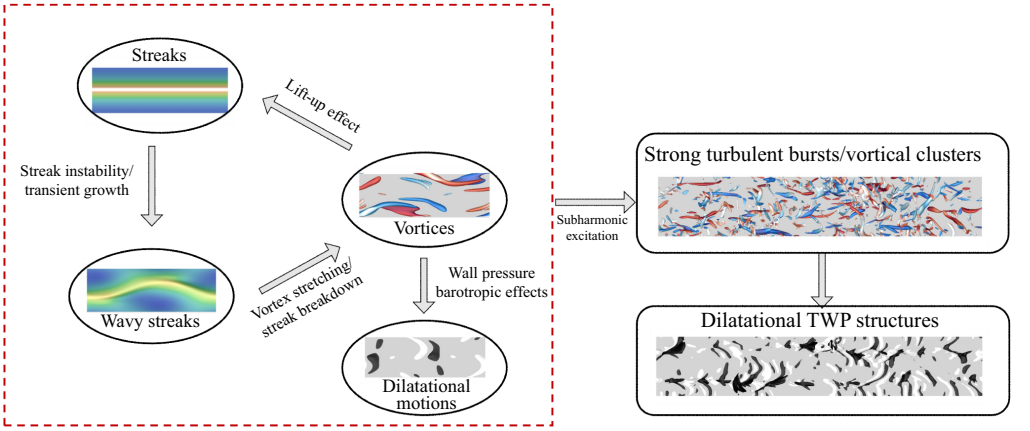

Figure 13. Summary of the near-wall self-sustaining cycles and the generation of the dilatational TWP structures.

are, at least partially, induced by the Orr mechanism, as proven by Lozano-Durán *et al.* (2021).

4. Concluding remarks

This paper explores the generation of dilatational motions in the form of travelling wave packets (TWPs), a gradually manifesting phenomenon with increasing Mach number and decreasing wall temperature, and its dynamical association with near-wall turbulence with the support of evidence of direct numerical simulations statistics, numerical experiments and theoretical analyses. Starting with the processes in the near-wall self-sustaining cycle, we eliminate the possibility of the generation of dilatational TWP structures being associated directly with the 'lift-up' effects inducing the low-speed streaks and the linear perturbation transient growth of the low-speed streaks – two physical processes that can be described by linear dynamics. The wall-normal velocity perturbations in the shape of TWPs close to the wall are not capable of triggering a high energy amplification rate in the framework of the stability of temporally steady streaks either. The initial weakly nonlinear stage of the streak evolution in numerical experiments reveals that the nonlinearity due to the parallel density and pressure gradients leads to the generation of dilatational structures with smaller streamwise length scales. The streak meandering and breakdown related to the Orr mechanism are accompanied by the vortical clusters that induce the strong wall pressure, and further, the dilatational TWPs excited by the aforementioned nonlinear effects. In fully developed turbulence, we found that the occurrence of the dilatational TWP structures should be attributed to the strong turbulent bursting events with wider spanwise scales and at higher locations. This is indicated by the much lower dilatational enstrophy if the wider and outer motions are removed artificially, and if the Orr mechanism, associated with the generation of the vortical clusters, is alleviated. In the strong shear environment with a high mean velocity gradient in the near-wall region, the wall-normal velocity induces spanwise-oriented shear and vorticity, which are responsible for the intensification of wall shear stress and wall heat flux fluctuations in high Mach number flows over cold walls (Yu *et al.* 2022*a*,*b*).

With the previous conclusions, we can summarize the descriptions of the dynamics of the generation of the dilatational TWP structures in the process of near-wall self-sustaining cycles in figure 13, and recapitulate it as follows. In the near-wall self-sustaining cycles, namely the regeneration between the velocity streaks and the vortical structures, the

dilatational TWP structures are induced during the vortex stretching and streak breakdown. The nonlinear effects of the inter-scale turbulent interaction and the Orr mechanism further lead to larger clusters of vortical motions. The strong vortical clusters lead to pressure fluctuations at the wall, which, due to the isothermal boundary condition, further result in similarly distributed density fluctuations. The approximately parallel pressure and density gradients generate pressure fluctuations and velocity divergence at smaller streamwise length scales through the strong nonlinear interaction, forming the dilatational structures organized as TWPs beneath the vortical clusters.

Funding. This work is supported by the National Natural Science Foundation of China (grant nos 12202469, 12388101 and 92052301).

Declaration of interests. The authors report no conflict of interest.

Author ORCIDs.
Ming Yu https://orcid.org/0000-0001-7772-833X;
ZiSong Zhou https://orcid.org/0000-0003-3708-1273;
SiWei Dong https://orcid.org/0000-0002-4725-2964;
XianXu Yuan https://orcid.org/0000-0002-7668-0116;
ChunXiao Xu https://orcid.org/0000-0001-5292-8052.

References

ADRIAN, R.J. 2007 Hairpin vortex organization in wall turbulence. *Phys. Fluids* **19** (4), 041301.
BARANWAL, A., DONZIS, D.A. & BOWERSOX, R.D.W. 2022 Asymptotic behaviour at the wall in compressible turbulent channels. *J. Fluid Mech.* **933**, A28.
BERNARDINI, M. & PIROZZOLI, S. 2011 Wall pressure fluctuations beneath supersonic turbulent boundary layers. *Phys. Fluids* **23** (8), 085102.
BOGARD, D.G. & TIEDERMAN, W.G. 1986 Burst detection with single-point velocity measurements. *J. Fluid Mech.* **162**, 389–413.
CASPER, K.M., BERESH, S.J. & SCHNEIDER, S.P. 2014 Pressure fluctuations beneath instability wavepackets and turbulent spots in a hypersonic boundary layer. *J. Fluid Mech.* **756**, 1058–1091.
CECI, A., PALUMBO, A., LARSSON, J. & PIROZZOLI, S. 2022 Numerical tripping of high-speed turbulent boundary layers. *Theor. Comput. Fluid Dyn.* **36** (6), 865–886.
COGO, M., SALVADORE, F., PICANO, F. & BERNARDINI, M. 2022 Direct numerical simulation of supersonic and hypersonic turbulent boundary layers at moderate-high Reynolds numbers and isothermal wall condition. *J. Fluid Mech.* **945**, A30.
DENG, B.-Q. & XU, C.-X. 2012 Influence of active control on STG-based generation of streamwise vortices in near-wall turbulence. *J. Fluid Mech.* **710**, 234–259.
DOOHAN, P., WILLIS, A.P. & HWANG, Y.Y. 2021 Minimal multi-scale dynamics of near-wall turbulence. *J. Fluid Mech.* **913**, A8.
DUAN, L., BEEKMAN, I. & MARTIN, M. 2010 Direct numerical simulation of hypersonic turbulent boundary layers. Part 2. Effect of wall temperature. *J. Fluid Mech.* **655**, 419–445.
DUAN, L., BEEKMAN, I. & MARTIN, M.P. 2011 Direct numerical simulation of hypersonic turbulent boundary layers. Part 3. Effect of Mach number. *J. Fluid Mech.* **672**, 245–267.
ENCINAR, M.P. & JIMÉNEZ, J. 2020 Momentum transfer by linearised eddies in turbulent channel flows. *J. Fluid Mech.* **895**, A23.
FEDOROV, A. 2011 Transition and stability of high-speed boundary layers. *Annu. Rev. Fluid Mech.* **43**, 79–95.
FLORES, O. & JIMÉNEZ, J. 2010 Hierarchy of minimal flow units in the logarithmic layer. *Phys. Fluids* **22** (7), 071704.
GATSKI, T. & BONNET, J. 2013 *Compressibility, Turbulence and High Speed Flow*. Academic Press.
GRIFFIN, K.P., FU, L. & MOIN, P. 2021 Velocity transformation for compressible wall-bounded turbulent flows with and without heat transfer. *PNAS* **118** (34), e2111144118.
HACK, M.J.P. & SCHMIDT, O.T. 2021 Extreme events in wall turbulence. *J. Fluid Mech.* **907**, A9.
HAMILTON, J.M., KIM, J. & WALEFFE, F. 1995 Regeneration mechanisms of near-wall turbulence structures. *J. Fluid Mech.* **287**, 317–348.

HUANG, J., DUAN, L. & CHOUDHARI, M.M. 2022 Direct numerical simulation of hypersonic turbulent boundary layers: effect of spatial evolution and Reynolds number. *J. Fluid Mech.* **937**, A3.

HWANG, Y.Y. & BENGANA, Y. 2016 Self-sustaining process of minimal attached eddies in turbulent channel flow. *J. Fluid Mech.* **795**, 708–738.

JIAO, Y., HWANG, Y. & CHERNYSHENKO, S.I. 2021 Orr mechanism in transition of parallel shear flow. *Phys. Rev. Fluids* **6** (2), 023902.

JIMÉNEZ, J. 2013 Near-wall turbulence. *Phys. Fluids* **25** (10), 101302.

JIMÉNEZ, J. 2018 Coherent structures in wall-bounded turbulence. *J. Fluid Mech.* **842**, P1.

JIMÉNEZ, J. & PINELLI, A. 1999 The autonomous cycle of near-wall turbulence. *J. Fluid Mech.* **389**, 335–359.

KIM, H.T., KLINE, S.J. & REYNOLDS, W.C. 1971 The production of turbulence near a smooth wall in a turbulent boundary layer. *J. Fluid Mech.* **50** (1), 133–160.

KIM, J. & MOIN, P. 1986 The structure of the vorticity field in turbulent channel flow. Part 2. Study of ensemble-averaged fields. *J. Fluid Mech.* **162**, 339–363.

KLEIN, M., SADIKI, A. & JANICKA, J. 2003 A digital filter based generation of inflow data for spatially developing direct numerical or large eddy simulations. *J. Comput. Phys.* **186** (2), 652–665.

LAGHA, M., KIM, J., ELDREDGE, J.D. & ZHONG, X. 2011 A numerical study of compressible turbulent boundary layers. *Phys. Fluids* **23** (1), 187.

LIANG, X. & LI, X.L. 2013 DNS of a spatially evolving hypersonic turbulent boundary layer at Mach 8. *Sci. China Phys. Mech. Astron.* **56**, 1408–1418.

LOZANO-DURÁN, A., CONSTANTINOU, N.C., NIKOLAIDIS, M.A. & KARP, M. 2021 Cause-and-effect of linear mechanisms sustaining wall turbulence. *J. Fluid Mech.* **914**, A8.

MACK, L.M. 1984 Boundary-layer linear stability theory. *AGARD Rep.* **709** (3), 1–3.

MORKOVIN, M.V. 1962 Effects of compressibility on turbulent flows. *Méc. Turbul.* **367** (380), 26.

ORR, W. 1907 The stability or instability of the steady motions of a perfect liquid and of a viscous liquid. Part II: A viscous liquid. In *Proceedings of the Royal Irish Academy. Section A: Mathematical and Physical Sciences*, vol. 27, pp. 69–138. JSTOR.

PIROZZOLI, S. & BERNARDINI, M. 2011 Turbulence in supersonic boundary layers at moderate Reynolds number. *J. Fluid Mech.* **688**, 120–168.

PIROZZOLI, S. & COLONIUS, T. 2013 Generalized characteristic relaxation boundary conditions for unsteady compressible flow simulations. *J. Comput. Phys.* **248**, 109–126.

ROBINSON, S. 1991 Coherent motions in the turbulent boundary layer. *Annu. Rev. Fluid Mech.* **23** (1), 601–639.

ROY, C.J. & BLOTTNER, F.G. 2006 Review and assessment of turbulence models for hypersonic flows. *Prog. Aerosp. Sci.* **42** (7–8), 469–530.

SCHOPPA, W. & HUSSAIN, F. 2002 Coherent structure generation in near-wall turbulence. *J. Fluid Mech.* **453**, 57–108.

SHARMA, B. & GIRIMAJI, S.S. 2023 Effect of flow–thermodynamics interactions on the stability of compressible boundary layers: insights from Helmholtz decomposition. *J. Fluid Mech.* **962**, A18.

SMITS, A.J. & DUSSAUGE, J.P. 2006 *Turbulent Shear Layers in Supersonic Flow*. Springer Science & Business Media.

STETSON, K. & KIMMEL, R. 1992 On hypersonic boundary-layer stability. In *30th Aerospace Sciences Meeting and Exhibit*, p. 737. AIAA.

TARDU, S. 1995 Characteristics of single and clusters of bursting events in the inner layer. *Exp. Fluids* **20** (2), 112–124.

THEOFILIS, V., PIROZZOLI, S. & MARTIN, P. 2022 Special issue on the fluid mechanics of hypersonic flight. *Theor. Comput. Fluid Dyn.* **36** (1), 1–8.

TICHENOR, N.R., HUMBLE, R.A. & BOWERSOX, R.D.W. 2013 Response of a hypersonic turbulent boundary layer to favourable pressure gradients. *J. Fluid Mech.* **722**, 187–213.

UNNIKRISHNAN, S. & GAITONDE, D.V. 2021 Instabilities and transition in cooled wall hypersonic boundary layers. *J. Fluid Mech.* **915**, A26.

WANG, Y.S., HUANG, W.X. & XU, C.X. 2015 On hairpin vortex generation from near-wall streamwise vortices. *Acta Mechanica Sin.* **31** (2), 139–152.

WILLIAMS, O.J.H., SAHOO, D., BAUMGARTNER, M.L. & SMITS, A.J. 2018 Experiments on the structure and scaling of hypersonic turbulent boundary layers. *J. Fluid Mech.* **834**, 237–270.

XU, C.X., DENG, B.Q., HUANG, W.X. & CUI, G.X. 2013 Coherent structures in wall turbulence and mechanism for drag reduction control. *Sci. China Phys. Mech. Astron.* **56**, 1053–1061.

XU, D., WANG, J., WAN, M., YU, C., LI, X. & CHEN, S. 2021*a* Compressibility effect in hypersonic boundary layer with isothermal wall condition. *Phys. Rev. Fluids* **6** (5), 054609.

XU, D., WANG, J., WAN, M., YU, C., LI, X. & CHEN, S. 2021*b* Effect of wall temperature on the kinetic energy transfer in a hypersonic turbulent boundary layer. *J. Fluid Mech.* **929**, A33.

YIN, G., HUANG, W. & XU, C. 2017 On near-wall turbulence in minimal flow units. *Intl J. Heat Fluid Flow* **65**, 192–199.

YU, M., LIU, P.X., FU, Y.L., TANG, Z.G. & YUAN, X.X. 2022*a* Wall shear stress, pressure and heat flux fluctuations in compressible wall-bounded turbulence. Part I. One-point statistics. *Phys. Fluids* **34** (6), 065139.

YU, M., LIU, P.X., FU, Y.L., TANG, Z.G. & YUAN, X.X. 2022*b* Wall shear stress, pressure and heat flux fluctuations in compressible wall-bounded turbulence, Part II: Spectra, correlation and nonlinear interactions. *Phys. Fluids* **34** (6), 065140.

YU, M. & XU, C.X. 2021 Compressibility effects on hypersonic turbulent channel flow with cold walls. *Phys. Fluids* **33** (7), 075106.

YU, M., XU, C.X. & PIROZZOLI, S. 2019 Genuine compressibility effects in wall-bounded turbulence. *Phys. Rev. Fluids* **4** (12), 123402.

YU, M., XU, C.X. & PIROZZOLI, S. 2020 Compressibility effects on pressure fluctuation in compressible turbulent channel flows. *Phys. Rev. Fluids* **5** (11), 113401.

ZHANG, C., DUAN, L. & CHOUDHARI, M.M. 2018 Direct numerical simulation database for supersonic and hypersonic turbulent boundary layers. *AIAA J.* **56** (11), 4297–4311.

ZHANG, P.J.Y., WAN, Z.H., LIU, N.S., SUN, D.J. & LU, X.Y. 2022 Wall-cooling effects on pressure fluctuations in compressible turbulent boundary layers from subsonic to hypersonic regimes. *J. Fluid Mech.* **946**, A14.

ZHANG, Y., BI, W., HUSSAIN, F. & SHE, Z. 2014 A generalized Reynolds analogy for compressible wall-bounded turbulent flows. *J. Fluid Mech.* **739**, 392–420.